JACS JOURNAL OF THE AMERICAN CHEMICAL SOCIETY

Article

pubs.acs.org/JACS

Oxygen "Getter" Effects on Microstructure and Carrier Transport in Low Temperature Combustion-Processed a-InXZnO (X = Ga, Sc, Y, La) Transistors

Jonathan W. Hennek,[†] Jeremy Smith,[†] Aiming Yan,[‡] Myung-Gil Kim,[†] Wei Zhao,[§] Vinayak P. Dravid,*[,‡] Antonio Facchetti,*[,†,§] and Tobin J. Marks*[,†,‡]

[†]Department of Chemistry and the Materials Research Center, Northwestern University, 2145 Sheridan Road, Evanston, Illinois 60208, United States

[‡]Department of Materials Science and Engineering and Materials Research Center, Northwestern University, 2220 Campus Drive, Evanston, Illinois 60208, United States

[§]Polyera Corporation, 8045 Lamon Avenue, Skokie, Illinois 60077, United States

S Supporting Information

ABSTRACT: In oxide semiconductors, such as those based on indium zinc oxide (IXZO), a strong oxygen binding metal ion ("oxygen getter"), X, functions to control O vacancies and enhance lattice formation, hence tune carrier concentration and transport properties. Here we systematically study, in the IXZO series, the role of X = Ga^{3+} versus the progression X = Sc^{3+} → Y^{3+} → La^{3+}, having similar chemical characteristics but increasing ionic radii. IXZO films are prepared from solution over broad composition ranges for the first time via low-temperature combustion synthesis. The films are characterized via thermal analysis of the precursor solutions, grazing incidence angle X-ray diffraction (GIAXRD), atomic force microscopy (AFM), X-ray photoelectron spectroscopy (XPS), and scanning transmission electron microscopy (STEM) with high angle annular dark field (HAADF) imaging. Excellent thin-film transistor (TFT) performance is achieved for all X, with optimal compositions after 300 °C processing exhibiting electron mobilities of 5.4, 2.6, 2.4, and 1.8 cm^2 V^{-1} s^{-1} for Ga^{3+}, Sc^{3+}, Y^{3+}, and La^{3+}, respectively, and with I_{on}/I_{off} = 10^7−10^8. Analysis of the IXZO TFT positive bias stress response shows X = Ga^{3+} to be superior with mobilities (μ) retaining >95% of the prestress values and threshold voltage shifts (ΔV_T) of <1.6 V, versus <85% μ retention and $\Delta V_T \approx 20$ V for the other trivalent ions. Detailed microstructural analysis indicates that Ga^{3+} most effectively promotes oxide lattice formation. We conclude that the metal oxide lattice formation enthalpy (ΔH_L) and metal ionic radius are the best predictors of IXZO oxygen getter efficacy.

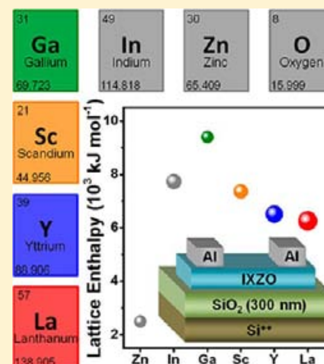

■ INTRODUCTION

The field of metal oxide semiconductors for thin-film transistor (TFT) implementation has experienced rapid progress, particularly after breakthroughs in amorphous oxide films less than a decade ago.[1] Owing to the their appreciable field-effect mobilities, smooth surfaces, and optical transparency, these materials are attractive for use in active-matrix organic light emitting diode (AM-OLED) displays, radio frequency ID tags, wearable sensor arrays, flexible displays, and flexible solar cells.[2] Very recently, several major manufacturers have begun full-scale production of displays using IGZO TFTs.[3] While amorphous silicon (a-Si:H) is currently utilized on a large scale in large-area electronics applications, it is limited by an intrinsically low field-effect mobility (<1 cm^2 V^{-1} s^{-1}), optical opacity, and marginal current-carrying capacity.[4] Organic semiconductors, including small molecules and polymers, carbon nanotubes (CNTs), and graphene have also enabled rapid advances in TFT performance.[1d,5] Although their performance continues to progress, many small molecules and polymers nevertheless suffer from relatively low electron mobilities (typically <2 cm^2 V^{-1} s^{-1}) and instabilities related to O_2, moisture, and light exposure.[6] CNT based TFTs have demonstrated good n- and p-type mobilities (~15 and 70 cm^2 V^{-1} s^{-1}, respectively)[7] as well as good current on:off ratios (I_{on}/I_{off}), but key issues such as large-scale chirality separation/targeted synthesis[8] and large-scale alignment[9] continue to present challenges. Graphene-based devices possess the highest mobilities, but have yet to demonstrate suitable "off" state currents, reflecting the negligible band gap.[5e,10]

In contrast to the aforementioned materials, metal oxide semiconductor films grown by physical vapor deposition techniques such as pulsed laser deposition[1g,11] and rf-magnetron sputtering[12] have shown mobilities exceeding 50 cm^2 V^{-1} s^{-1}, I_{on}/I_{off} exceeding 10^7, and stable threshold voltages (V_T) near 0 V. In fact, multiple display manufacturers have recently announced large-scale production of AM-OLED and liquid crystal displays (LCDs) using amorphous indium gallium zinc oxide (a-IGZO) based TFTs.[13] For these reasons, solution

Received: April 10, 2013
Published: July 2, 2013

ACS Publications © 2013 American Chemical Society

processing of transparent oxide films becomes an especially attractive, low-cost, high-throughput, and low materials waste alternative to physical vapor deposition film growth techniques.[1b] Furthermore, solution processing offers simple and broad tuning of composition, whereas most vapor phase techniques require costly target fabrication with each desired composition modification. Spin-coating,[14] chemical bath deposition,[15] gravure printing,[16] and inkjet printing[17] have all been extensively studied as oxide solution deposition methods, with the goal of ultimately achieving efficient roll-to-roll device fabrication. However, until recently, typical solution-based routes to functional metal oxide films have required an extremely high temperature annealing step (≥400 °C) to promote metal−oxygen−metal (M−O−M) lattice formation, densification, and impurity removal. Recently, Banger and co-workers introduced rationally designed metal alkoxide precursors that, when spin-coated and annealed, undergo hydrolysis and condensation at low temperatures (200−250 °C) to enable good M−O−M formation.[18] Nevertheless, this approach requires time-consuming and expensive synthesis of a different metal−organic precursor for each metal ion.

We recently reported a general approach to low temperature solution processing of functional metal oxide films called combustion synthesis (Figure 1).[19] By introducing an oxidizer

Figure 1. (A) Schematic reaction coordinate comparing the energetics for combustion synthesis and conventional sol−gel solution processing. (B) Example of combustion reaction for a generic metal with nitrate acting as the oxidizer and acetylacetone as the fuel.

(in the form of a metal nitrate salt) and a fuel (acetylacetone or urea) into the precursor solution, the chemical potential of the oxide precursor is greatly enhanced. When spin-coated and annealed, a highly exothermic but local chemical transformation occurs within the film, leading to rapid and efficient condensation and M−O−M lattice formation at low external input temperatures (i.e., via a hot plate or oven). Owing to the large surface area/volume ratio of these films, heat is readily dissipated and is therefore not detrimental to the underlying substrate, meaning that this process is compatible with several types of low-cost plastic substrate. To date, we have shown combustion synthesis to be an effective method to explore new functional semiconducting metal oxides,[20] and as an electronic binder in transparent conducting oxide nanoparticle films.[21]

The aforementioned interest in semiconductor metal oxide electronics stems from the distinctive electronic structures of these materials versus silicon. In a-Si:H, the conduction band primarily consists of covalent sp^3 hybridized orbitals with many tail states present in the gap due to dangling bonds, impeding transport and making it extremely sensitive to lattice distortion and processing. For these reasons, a-Si:H exhibits a ~1000-fold reduction in mobility versus the crystalline state.[4] In contrast, for metal oxide semiconductors, conduction is relatively insensitive to lattice distortion because the conduction band states are principally derived from spherical metal s-orbitals with electronic structure $(n-1)d^{10}ns^0$ where $n \geq 5$ (e.g., in Sn^{4+}, Cd^{2+}, In^{3+}).[22] The exact mechanism of free carrier (electron) generation in these oxides is currently the subject of extensive literature discussion.[2c,23] In crystalline metal oxides, some experimental data and first-principles theoretical calculations predict that antisite defects (e.g., $In^{\bullet}_{Zn}$ for $In_2O_3(ZnO)_3$) act as shallow donors while oxygen vacancies occupy deep levels in In_2O_3, ZnO, and $InGaO(ZnO)_k$, constituting deep traps.[24] On the other hand, theoretical studies on amorphous oxides have shown that the local environment influences whether an oxygen vacancy will act as a deep trap or shallow donor.[23a] In addition, several studies have shown that oxygen vacancies play a major role in the instability properties of a-IGZO.[23a,25] Binary polycrystalline metal oxide semiconductors such as SnO_2,[25] In_2O_3,[26] and ZnO[27] exhibit very high electron mobilities when subjected to moderate to high temperature annealing. However, the major shortcomings of these binary oxides are (1) achieving high levels of crystallization to yield high mobility at lower temperatures, (2) poor control of defects leading to high off-currents in some cases, and (3) grain boundaries causing electrical inhomogeneities as well as structural defects which can promote film cracking on flexible substrates. To suppress crystallization, ternary oxide semiconductors have been prepared by a variety of solution and vapor deposition techniques. Indium zinc oxide (IZO),[26] indium tin oxide (ITO),[14a] aluminum indium oxide (AIO),[27] and zinc tin oxide (ZTO)[28] are among the most promising candidates in terms of achieving high mobility, in the range of 1 to 20 $cm^2\ V^{-1}\ s^{-1}$, depending on deposition and postprocessing techniques. However, while it is possible to achieve high mobilities with ternary oxides, they often suffer from severe bias, light, and environmental instabilities, limiting their potential applications. Nomura et al. first introduced gallium into IZO,[1g] which has subsequently been shown to promote amorphicity, thereby eliminating grain boundaries, controlling carrier concentration, and increasing resistance to various instabilities by reducing the film metal hydroxide (M−OH) and oxygen vacancy content. Subsequently, numerous other "oxygen getters" have been investigated; that is, metal ions which have a strong oxygen affinity, including Ti^{4+},[29] W^{6+},[30] Gd^{3+},[31] Sr^{2+},[32] Si^{4+},[33] Zr^{4+},[34] Hf^{4+},[35] Sc^{3+},[36] Y^{3+},[37] and La^{3+}.[38]

In this contribution, we employ combustion synthesis to prepare several series of amorphous quaterny metal oxide semiconductors of type a-InXZnO (X = Ga, Sc, Y, La) and explore the effect(s) of various "oxygen getter" metal ions with respect to undoped InZnO. Specifically, we compare and contrast the thin film properties of Ga^{3+}, the most widely studied getter cation, with those of the group 3/lanthanide ions, Sc^{3+}, Y^{3+}, and La^{3+}, which have similar chemical properties but differ greatly in ionic radius. While several studies have addressed the doping properties of these cations individually, to our knowledge this is the first time that more than one getter ion is studied under identical processing conditions in order to understand how their incorporation into the InZnO lattice affects a-InXZnO charge transport properties. Here we present a detailed structure−function investigation utilizing precursor solution thermal analysis, combined with thin film grazing incidence X-ray diffraction, atomic force microscopy, X-ray photoelectron spectroscopy, and scanning transmission electron microscopy with high angle annular dark field imaging of the resulting films, followed by thin-film transistor (TFT) transport analysis, including bias-stress studies. Owing to the versatility and efficiency of the combustion synthesis approach,

dx.doi.org/10.1021/ja403586x | J. Am. Chem. Soc. 2013, 135, 10729−10741

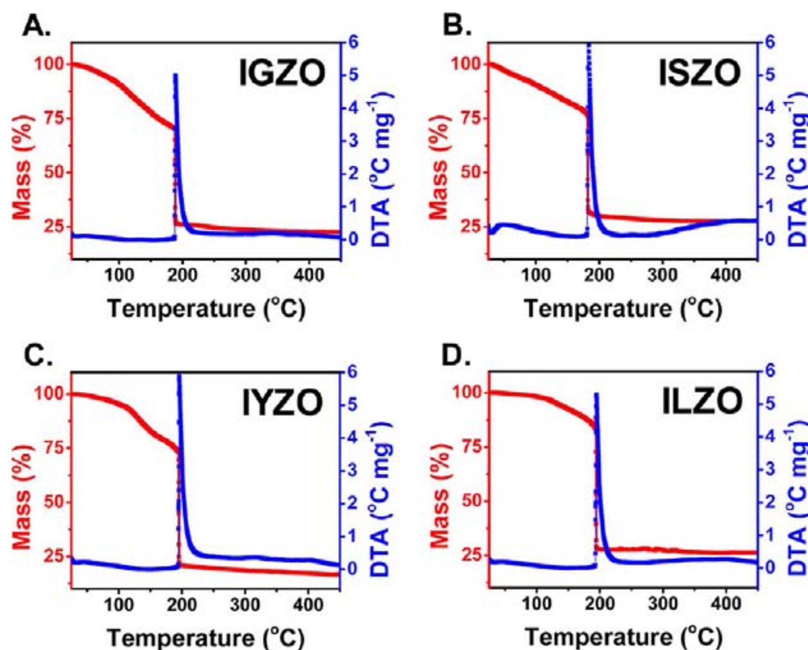

Figure 2. Thermogravimetric analysis (TGA, left axis) and differential thermal analysis (DTA, right axis) of IXZO combustion precursor solutions with atomic ratio In:X:Zn = 72.5:7.5:20. (A) X = Ga, (B) X = Sc, (C) X = Y, and (D) X = La. Sharp mass loss and large exothermic peaks can be seen in all cases at ~190 °C.

these metal oxide semiconductor films can be grown using processing temperatures (T_{anneal} = 250 and 300 °C) significantly lower than the 450−550 °C typically used for solution-processed ISZO, IYZO, and ILZO TFTs.[36a,37,38] Thus, IGZO TFTs fabricated by combustion processing are demonstrated for the first time and shown to exhibit excellent mobilities >5 cm^2 V^{-1} s^{-1} and good bias-stress stability for moderate film thermal processing at 300 °C, well within the T_g's of many commercially available transparent polymer substrate materials. Finally, we present metal oxide lattice enthalpies and ionic radii as predictive parameters for oxygen getter efficacy and provide candidates for future exploration.

■ RESULTS

To investigate the function of the oxygen getter in the InXZnO quaternary amorphous oxide semiconductor system (X = Ga^{3+}, Sc^{3+}, Y^{3+}, and La^{3+}), we first analyze the thermal characteristics of the combustion precursors for each materials system. Next, thin films are grown over a large composition range of the phase space diagram to systematically assay the effects of each metal constituent on morphology and charge transport characteristics for films annealed at two temperatures (T_{anneal} = 250 and 300 °C). To elucidate any structural differences between the systems, diverse characterization techniques are employed. Grazing incidence angle X-ray diffraction (GIAXRD) is performed to verify the amorphous microstructure, and atomic force microscopy (AFM) to probe surface morphology. Scanning transmission electron microscopy (STEM) with high angle annular dark field (HAADF) imaging is next used to characterize the microstructures of these films, and X-ray photoelectron spectroscopy (XPS) is performed to assess the oxygen bonding states within the films. TFTs are then fabricated and evaluated under all conditions to correlate transport properties with the thin film electronic structure and microstructure. Finally, bias stress measurements are performed to assess the stabilizing efficacy of each oxygen getter during actual TFT operating conditions.

Thermal Analysis of Combustion Precursor Synthesis. Thermogravimetric analysis (TGA, left axis) and differential thermal analysis (DTA, right axis) data for representative combustion IXZO precursor compositions are shown in Figure 2. These compositions are those affording, upon thermal conversion, optimal TFT device performance. Samples for thermal analysis are prepared by mild drying under vacuum of 0.05 M combustion precursor solutions comprised of a metal nitrate in 2-methoxyethanol with acetylacetone as the fuel, and ammonia as a chelating/hydrolyzing agent (see Experimental Section for details). As a consequence of this procedure, the initial mass loss differences between the samples are due to residual solvent variations. However, all of the four systems undergo an abrupt and complete mass loss at ~190 °C, corresponding to the onset of combustion, and corresponding to a very sharp exotherm in the DTA. The complete mass loss at T_{anneal} < 200 °C is significant, especially when compared to conventional sol−gel routes where decomposition and dehydration are typically followed much later/at higher temperatures by extensive dehydroxylation, finally followed by densification.[39] In the present case, densification occurs as T_{anneal} is increased, but extensive dehydroxylation is not observed.

IXZO Thin Film Growth and Microstructure. Figure 3b shows the phase space diagram for the quaternary oxides investigated in this study. Based on other studies on crystalline and amorphous oxide semiconductors,[40] it is predicted that as the concentration of X increases, the TFT field-effect mobility will fall because the conduction band primarily consists of In^{3+} 4s-states.[22a,41] Thus, for high levels of X doping, the electron transport is expected to degrade severely. For this reason, in order to compare film microstructure and charge transport efficiency, predominantly In-rich films were examined, while varying the Zn^{2+} composition at total metal concentration

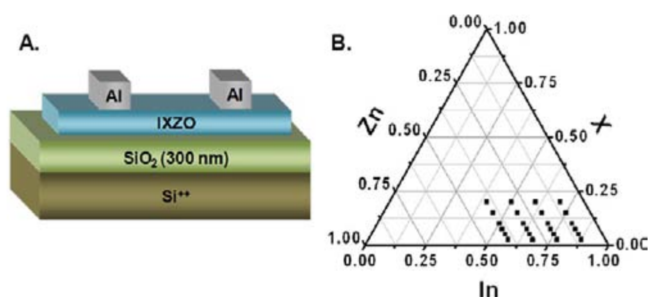

Figure 3. (A) Bottom-gate top-contact thin-film transistor geometry utilized in this study and (B) phase space investigated for IXZO, where X = Sc, Ga, Y, or La and T_{anneal} is both 250 and 300 °C.

intervals of 10 atom % (i.e., 10, 20, 30, and 40 atom %), while making smaller variations in the X^{+3} content (2.5, 5, 7.5, 10, 15, and 20 atom %). The T_{anneal} values selected for this study are 250 and 300 °C in order to demonstrate processing that is compatible with inexpensive plastic substrates and, while based on previous work,[20] maximizing TFT electrical performance. IXZO thin films were grown from precursor solutions of 0.05 M metal nitrate salts in 2-methoxyethanol, combining them with acetylacetone as fuel and ammonia as a complexing agent, and then allowing them to stir/age for 12 h. Approximately 1 h prior to spin-coating, the combustion precursor solutions for the desired metals were combined by micropipet to the desired atomic ratios and stirred. The IXZO precursor solutions were then spin-coated on Si/SiO_2 substrates and annealed at the desired temperature. This spin-coating process was repeated three additional times to afford film thicknesses of ~12 nm, as measured by spectroscopic ellipsometry (see Experimental Section for full details).

Representative GIAXRD plots for IXZO films annealed at 300 °C are shown in Figure 4; the entire GIAXRD data set can

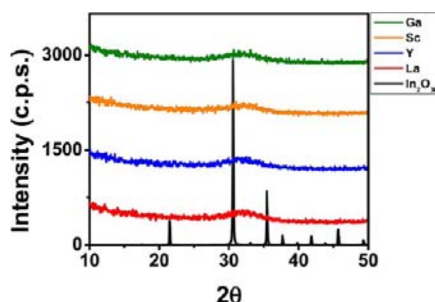

Figure 4. Grazing incidence angle X-ray diffraction patterns of IXZO thin films (In:X:Zn = 72.5:7.5:20 atom %; T_{anneal} = 300 °C) on Si substrates demonstrating their amorphous nature. Additional X-ray data can be found in the Supporting Information.

be found in Figures S1−S8 (Supporting Information). From these plots it is clear that, regardless of the oxygen getter, all films are essentially amorphous at a macroscopic level, independent of the composition or annealing temperature. This result is in accord with previous studies showing that minimal amounts of Y^{3+} added to In_2O_3 are sufficient to frustrate crystallization, leading to an amorphous microstructure.[20]

Scanning transmission electron microscopy (STEM) high angle annular dark field (HAADF) images of four free-standing IXZO films annealed at 300 °C are shown in Figure 5, along with their typical energy-filtered diffraction patterns (inset).

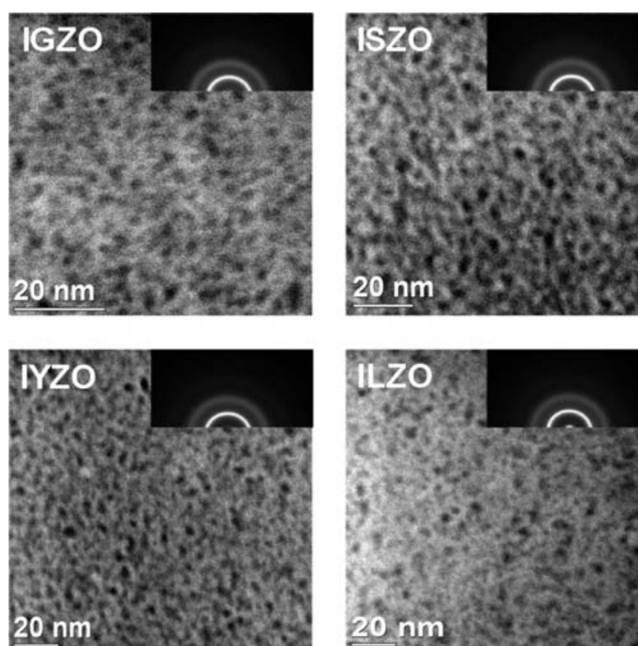

Figure 5. STEM-HAADF images for free-standing IXZO films with atom % ratio In:X:Zn = 72.5:7.5:20 at 300 °C. Inset: Energy-filtered electron diffraction patterns for free-standing IXZO films with *d*-spacing calibrated using a polycrystalline gold film prepared by thermal evaporation.

The diffuse diffraction rings in all four diffraction patterns support the local and spatially consistent amorphous nature of these thin films as also detected above by XRD averaged over the entire film. In the HAADF images, the dark contrast denotes areas of lower mass density than the surrounding gray or white matrix since HAADF imaging is insensitive to diffraction and phase contrast. Thus, because the films lack long-range order, the spatially distributed "dark-gray-white" contrast indicates that the films are nanoporous, similar to what is commonly observed in conventional sol−gel materials, including sol−gel-derived semiconductors.[42] During the annealing of solution/sol−gel processed oxides, the metal−organic precursors decompose with gas evolution, typically CO_2, H_2O, N_2, and/or O_2, affording nanoporous structures similar to those shown in Figure 5.[43] For example, Chung et al. described sol−gel derived a-IGZO TFTs with pores on the scale of ~5 nm as determined by TEM.[44] Furthermore, they reported detailed electrical characterization in vacuum and after heating, revealing that the porous nature of a-IGZO enables excess O_2 adsorption, exacerbating threshold voltage shifts under bias stress.[44] The measured average pore sizes in the four films of Figure 5 are in the range of 2−6 nm. Nevertheless, these combustion-derived films are suitable for device applications, plausibly because the multilayer deposition process provides contiguous charge transport pathways (see more below).

Thin Film Morphology and Chemical Composition. AFM images were acquired for representative IXZO and IZO films annealed at both 250 and 300 °C (Figures 6 and S9), revealing extremely smooth, featureless morphologies characterized by root-mean-square (RMS) roughness values of <0.2 nm. These findings are in accord with our previous reports of the very smooth character of combustion-processed In_2O_3 and binary oxide films.[19−21]

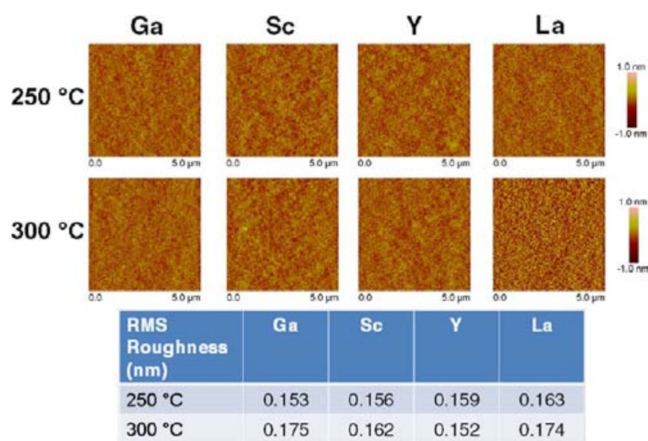

RMS Roughness (nm)	Ga	Sc	Y	La
250 °C	0.153	0.156	0.159	0.163
300 °C	0.175	0.162	0.152	0.174

Figure 6. Representative atomic force micrographs (AFMs) and RMS roughness values of combustion-derived IXZO films with atom ratios: 72.5:7.5:20 processed at 250 and 300 °C and exhibiting extremely smooth surface morphologies.

X-ray photoelectron spectroscopy was next performed on the IXZO films to better understand the chemical and local bonding structural differences among the present quaternary oxides. The oxygen 1s spectra can be deconvoluted into three principal signatures: (1) M−O−M lattice species at 529.8 ± 0.1 eV, (2) bulk and surface metal hydroxide (M−OH) species at 531.1 ± 0.1 eV, and (3) weakly bound (M−OR) species such as H_2O or CO_2 at 532.2 ± 0.1 eV.[45] As in the GIAXRD analysis, the XPS spectra were obtained for both low (2.5 atom %) and high (20 atom %) X concentrations at Zn = 10, 20, 30, and 40 atom % and for films lacking an oxygen getter (IZO) for film annealing at both 250 and 300 °C. Figure 7 shows representative O1s spectra (black line) for two IXZO compositions (X = Ga, Y), where the red line is the fitted profile with the deconvoluted peaks of the binding energies (blue) for the three relevant chemical components. Here, the increase in M−O−M lattice species as Ga concentration increases from 2.5 to 20 atom % is evident. In the case of Y, the trend is the inverse. The remaining spectra, peak positions, FWHMs, areal fractions, and reduced χ^2 data can be found in Figures S10−S17 and Tables S1−S5 of the Supporting Information. All XPS spectra were fitted using Gaussian−Lorentzian product functions after subtracting the baseline, and the peak positions were fixed within the ranges specified above. Charge transport in metal oxide semiconductors relies on extensive M−O−M lattice formation.[23a,c] Furthermore, metal hydroxide (M−OH) and surface adsorbed carbon species (M−OR) are well-known electron traps in solution-processed oxide films.[46] In order to achieve high mobility and maintain a low threshold voltage, a good semiconductor should maximize M−O−M formation and minimize detrimental M−OH and M−OR contributions. Thus, an instructive comparison to understand device performance is to compare the XPS O1s subpeak ratio of the lowest energy M−O−M peak area to the total O1s peak area, defined here as $\eta_{\text{M-O-M}}$. An effective 'oxygen getter' should *increase* this ratio.

Figure 8 details the $\eta_{\text{M-O-M}}$ ratio as the Zn atomic concentration is varied for low and high X atom concentrations for both 250 (A) and 300 °C (B) combustion-processed films. For low doping levels (2.5%) the difference in $\eta_{\text{M-O-M}}$ between the four semiconductors is quite small. This is expected since the total composition variation between each film is minimal. The $\eta_{\text{M-O-M}}$ variation that is observed reflects a combination of the differences in surface chemistry of each oxide and the small variability in the level of surface "contamination" found on each film. Previous XPS studies have shown that the magnitude of

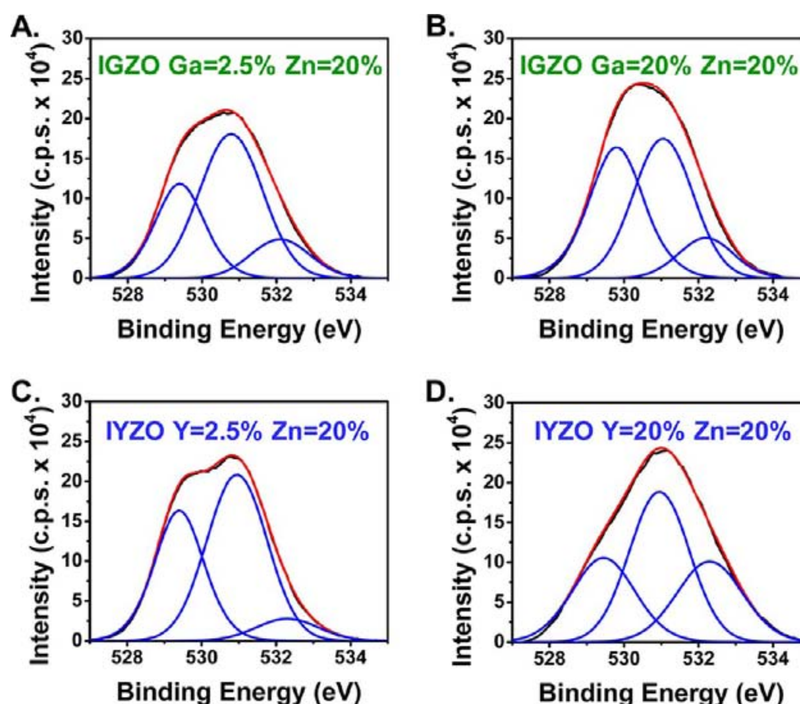

Figure 7. Representative O1s photoelectron spectra (XPS) of IGZO and IYZO thin film at T_{anneal} = 250 °C including Gaussian fits to three peaks representing M−O−M oxygen lattice species (529.8 ± 0.1 eV), metal hydroxide oxygen (531.1 ± 0.1 eV), and adsorbed oxygen species (532.2 ± 0.1 eV). For IGZO, increased oxygen getter concentration leads to an increase in $\eta_{\text{M-O-M}}$ while in IYZO a decrease of $\eta_{\text{M-O-M}}$ is observed for increasing Y concentration.

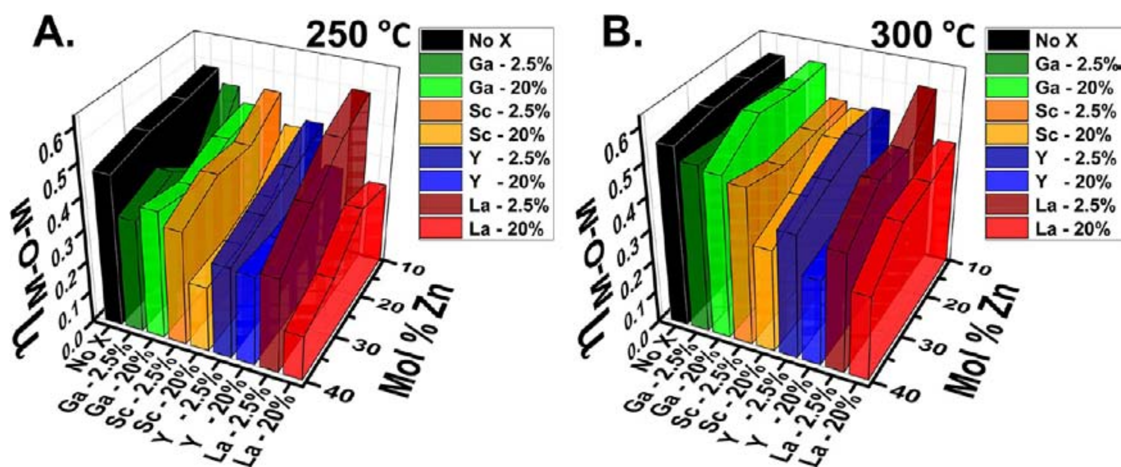

Figure 8. Ratio of the O1s metal−oxygen−metal peak area to the total peak area ($\eta_{M\text{-}O\text{-}M}$) for XPS O1s spectra fitted as shown in Figure 7 for both low (2.5%) and high (20%) X concentrations as the Zn concentration is varied where X = Ga, Sc, Y, La, and no X for (A) 250 and (B) 300 °C processing temperatures.

surface bound species is oxide dependent,[47] and so at high X doping levels, the surface chemistry differences, as well as the changes to the oxide lattice, will be observed. For example, Y_2O_3 is known to be basic and will have a greater degree of reactivity with CO_2 and other carbonaceous compounds than Ga_2O_3.[48] The unique reactivity of yttria is illustrated in Figures S14 and S15 by the large increase in the adsorbed surface species subpeak (∼532.2 eV) when the yttrium concentration is increased from 2.5% to 20%. Furthermore, the effect of back channel adsorbed and/or bound species on charge transport has been well established for oxide electronics.[49] Thus, the analysis of the M−OH and M−OR subpeaks in relation to the M−O−M subpeak is extremely useful when correlating XPS data to FET electron transport in metal oxide semiconductors. At the lower T_{anneal} = 250 °C a general trend is that as the atomic concentration of Zn increases, $\eta_{M\text{-}O\text{-}M}$ decreases. Furthermore, this ratio is relatively insensitive to Ga incorporation (shown in green) in the oxide lattice, while Sc (orange), Y (blue), and La (red) incorporation leads to a significant decrease. At T_{anneal} = 300 °C, high Ga content does afford increased $\eta_{M\text{-}O\text{-}M}$ content. Again Sc, Y, and La addition all cause $\eta_{M\text{-}O\text{-}M}$ to decrease. These results are important and rather surprising since, of the four oxygen getters addressed in this study, only Ga acts to cumulatively enhance metal oxide lattice formation as it is integrated into the film (*vide infra*). In addition, XPS analysis of films without an oxygen getter (IZO) reveals very little variation in $\eta_{M\text{-}O\text{-}M}$ with increased Zn atomic content and an expected increase in $\eta_{M\text{-}O\text{-}M}$ upon increasing T_{anneal} from 250 to 300 °C. When comparing IZO to the IXZO systems it is important to note that the introduction of an additional cation (X), while controlling the oxygen vacancy concentration, will also introduce an additional source of structural disorder.[1c] Therefore, for a fixed annealing temperature, a ternary oxide lattice will form more easily than a quaternary lattice. This leads to generally higher values of $\eta_{M\text{-}O\text{-}M}$ for IZO compared to IXZO at constant Zn concentration. In practice, this means that there is no ideal control oxide system (i.e., a film with no getter but also having the same level of structural disorder) for correlating the two oxide systems.

Thin-Film Transistor Fabrication and Electrical Characterization. To investigate how IXZO film composition affects film charge transport properties, bottom-gate top-contact thin-film transistors were fabricated on p^+-Si/SiO_2 (300 nm) wafers. Figure 3 shows the device architecture (A) and the metal composition space (B) of the TFTs fabricated for semiconductor channels, annealed at both 250 and 300 °C. Thermally evaporated Al, patterned through a shadow mask, was used as the source and drain electrodes to afford channel dimensions of L = 100 and W = 5000 μm. These dimensions were carefully selected to ensure accurate determination of the field-effect mobility.[50] Furthermore, the IXZO films were etched/patterned with oxalic acid prior to electrode deposition to eliminate the effects of parasitic currents arising from the common gate structure. TFT transfer characteristics were obtained for all IXZO compositions and for films annealed at both temperatures. The field-effect mobility (μ_{sat}) was calculated from the slope of $I_{DS,\,sat}^{1/2}$ vs V_G according to the conventional thin film transistor model (eq 1) in the saturation regime. Here C_i is the capacitance of the gate insulator (11 nF/cm^2 for the 300 nm SiO_2 used here), and L and W are the channel length and width,

$$\mu_{sat} = \left(\frac{\partial\sqrt{I_{DS}}}{\partial V_G}\right)^2 \frac{2L}{WC_i} \tag{1}$$

respectively (see Experimental Section for details). Table 1 summarizes representative TFT performance parameters for the IXZO compositions affording optimum performance. Note that identical TFTs were also fabricated utilizing IZO channels

Table 1. Representative TFT Performance for IXZO Film Combustion Processed at 250 and 300 °C

X	T_{Anneal} (°C)	optimized composition (In:X:Zn atom %)	μ_{sat} ($cm^2\,V^{-1}\,s^{-1}$)	V_T (V)	I_{on}/I_{off}
Ga	250	85:5:10	1.28	25	10^7
	300	80:10:10	5.43	17	10^8
Sc	250	77.5:2.5:20	0.45	16	10^7
	300	77.5:2.5:20	2.57	29	10^8
Y	250	87.5:2.5:10	0.35	22	10^8
	300	87.5:2.5:10	2.37	16	10^7
La	250	77.5:2.5:20	0.65	23	10^8
	300	87.5:2.5:10	1.81	25	10^7
none	250	70:0:30	0.42	52	10^6
	300	70:0:30	5.72	17	10^8

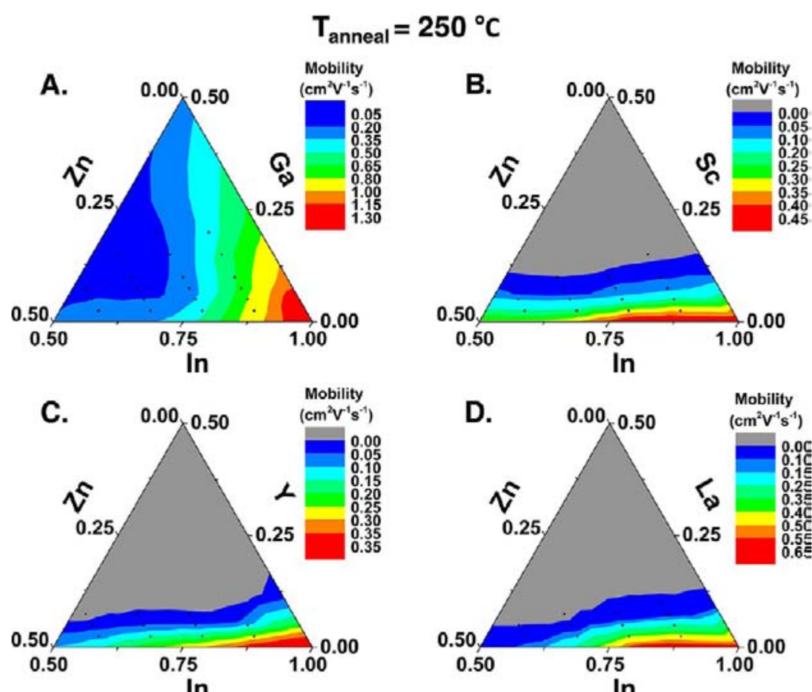

Figure 9. Field-effect mobility trends extracted from TFT transfer characteristics for IXZO devices fabricated at 250 °C with the metal concentrations indicated by the data points. Light gray shaded region represents inactive devices. Note that scales vary for each plot.

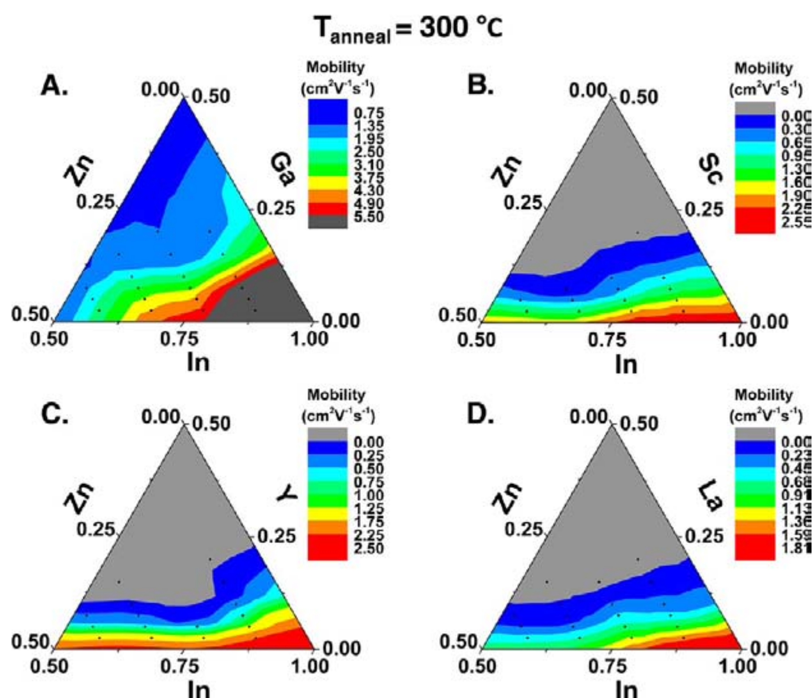

Figure 10. Field-effect mobility trends extracted from TFT transfer characteristics for IXZO devices processed at 300 °C and having the indicated metal concentrations. The light gray shaded regions represent inactive devices while dark gray region represents always-on samples. Note that scales vary for each plot.

as control devices to confirm concurrence with previous results.[19] In agreement with previous findings, IZO TFTs fabricated at T_{anneal} of 250 °C exhibit a mobility ranging from 0.14 to 1.01 cm^2 V^{-1} s^{-1} while those fabricated at T_{anneal} = 300 °C achieve mobilities in the range of 3.89 to 8.69 cm^2 V^{-1} s^{-1}, depending on Zn content (Table S6). From these data it is clear that the field-effect mobility increases when the annealing temperature is increased and ranges from 0.35 (X = Y) to 1.28 cm^2 V^{-1} s^{-1} (X = Ga) for T_{anneal} = 250 °C and from 1.81 (X = La) to 5.43 cm^2 V^{-1} s^{-1} (X = Ga) for T_{anneal} = 300 °C. Interestingly, both the threshold voltage (V_T) and the on−off current modulation (I_{on}/I_{off}) are far less sensitive to either the annealing temperature or composition and remain in the ranges ~15−30 V and ~10^7−10^8, respectively. Note that the moderately high V_T values for these TFTs are the result of

the relatively thick SiO_2 (300 nm) dielectric layer, thin a-IXZO active layers, and a nonoptimal device architecture.[51]

To scrutinize the effects of the elemental composition on the IXZO TFT charge transport, we focus first on the field-effect mobility trends as shown in Figures 9 (T_{anneal} = 250 °C) and 10 (T_{anneal} = 300 °C). Note that these mobility values are averaged from at least four transistors per composition. In these plots, light gray represents areas where IXZO compositions afford inactive TFTs whereas dark gray represents highly conductive devices that cannot be switched off upon application of a large negative gate bias. IGZO TFTs annealed at 250 °C (Figure 9A) function properly up to 20 atom % Ga, regardless of the Zn concentration. However, as the Ga concentration is increased further, the mobility degrades from a maximum of >1 cm^2 V^{-1} s^{-1} to < 0.1 cm^2 V^{-1} s^{-1} for In:Ga:Zn = 40:20:40. In comparison, for ISZO TFTs (B) processed at the same temperature, a maximum mobility of ~0.5 cm^2 V^{-1} s^{-1} is obtained at In:Sc:Zn = 87.5:2.5:10. As the Sc content is increased, a sharp drop in mobility is observed until the Sc content is increased above 10 atom %, at which point the TFTs no longer function. Similar trends are observed for both IYZO (C) and ILZO (D), where devices reach a maximum mobility of 0.35 and 0.65 cm^2 V^{-1} s^{-1}, respectively. As with ISZO TFTs annealed at the same temperature, a relatively abrupt drop in mobility is observed for IYZO and ILZO, with films becoming insulating around 10−15 atom % Y and La. A clear trend evident in the group 3 metals is that as the oxygen getter ion size increases from Sc^{3+} to Y^{3+} to La^{3+}, the TFTs become inactive at lower X doping content. This is likely related to structural disorder caused by the larger Y^{3+} and La^{3+} ions disrupting the lattice.

When the processing temperature is increased to 300 °C, a marked increase in mobility is observed for the IGZO TFTs (Figure 10A). In fact, for Zn = 10 atom % and Ga = 2.5, 5, and 7.5 atom % compositions, the IGZO TFTs become too conductive to be properly modulated by the gate bias and to meaningfully extract μ_{sat}. However, upon higher levels of Ga and/or Zn incorporation (Ga ≥ atom 10% for Zn = 10 atom % and Ga ≥ 2.5 atom % when Zn ≥ 20 atom %), good gate modulation and excellent mobilities are observed, up to 5.4 cm^2 V^{-1} s^{-1} and dropping to 0.75 cm^2 V^{-1} s^{-1} in the case of very low In contents (In:Ga:Zn = 40:20:40). In marked contrast, ISZO, IYZO, and ILZO all exhibit similar compositional trends in carrier mobility with a clear variation observed depending on metal ionic radius (Figure 10B−D). That is, as the X^{+3} eight-coordinate ionic radius[52] increases from 0.89 Å (Sc^{3+}) to 1.04 Å (Y^{3+}) to 1.17 Å (La^{3+}), the highest achievable mobility decreases from ~2.6 cm^2 V^{-1} s^{-1}, to 2.5 cm^2 V^{-1} s^{-1}, to 1.8 cm^2 V^{-1} s^{-1}, respectively. Again, the IXZO TFTs based on the X = non-Ga^{3+} metals do not function when the X doping concentration is increased beyond 10−15 atom %. The overall TFT performance enhancement for T_{anneal} = 300 °C versus 250 °C is not surprising and likely reflects increased hydrolysis, densification, and structural relaxation, specifically related to replacement of weak Zn−O bonds (see Discussion).[2c,53]

Overall, very good mobility values are obtained for all of the present combustion-processed IXZO film systems. While conventional sol−gel processed IGZO films typically exhibit $\mu_{sat} \approx 1$ cm^2 V^{-1} s^{-1} for T_{anneal} = 400 °C, the combustion route yields similar values for processing temperatures of only 250 °C.[54] Note that, at T_{anneal} = 300 °C, Banger et al. also demonstrated a mobility of ~5 cm^2 V^{-1} s^{-1} using somewhat less straightforward metal−organic precursors and processing.[18]

Previous reports of introducing Sc into IZO required T_{anneal} = 500 °C to obtain functioning TFTs with a maximum mobility of ~2.1 cm^2 V^{-1} s^{-1}, while, with combustion synthesis, a slightly greater mobility of ~2.6 cm^2 V^{-1} s^{-1} is possible at a significantly lower T_{anneal} = 300 °C.[36a] Similarly, other reports of IYZO and ILZO films utilized conventional sol−gel approaches with T_{anneal} ~550 °C to yield TFTs with μ_{sat} = 1.1 and 2.6 cm^2 V^{-1} s^{-1}, respectively.[37,38]

Thin-Film Transistor Bias Stress Properties. To be useful in TFTs, an effective semiconducting channel material must be stable under constant bias stress.[55] Previous reports have shown that metal oxide semiconductor performance under bias stress is related to a variety of factors, including H_2O and O_2 adsorption on the back channel and electron trapping at the semiconductor/dielectric interface.[56] For thin semiconductor films (as in the present case), H_2O adsorption has been shown to create an accumulation layer due to electron donation, resulting in a negative V_T shift.[46] On the other hand, O_2 adsorption is known to form a depletion layer below the active surface, leading to a positive V_T shift.[44] Unlike trapping at the semiconductor/dielectric interface, these two factors can be mitigated by appropriate passivation of the channel. This is often accomplished by sputter coating the film with inorganic materials such as SiN_x[57] or TiO_x,[58] or spin-coating organic layers such as SU-8[59] or CYTOP.[60] The second cause of bias induced instability however is thought to be related in large part to induced O defect states in the material, generated by high voltage bias.[61] Thus, an effective channel material should have resiliency to O defect related instabilities.

To compare the properties of the different IXZO channel materials, TFTs were fabricated as described previously (here channel L = 50, W = 1000 μm; see Experimental Section for details) with In:X:Zn = 72.5:7.5:20 atom % or 70:0:30 (see Supporting Information) and T_{anneal} = 300 °C. These devices were then subjected to a V_G−V_D constant bias of +20 V for 200 s intervals for the duration of 1200 s in ambient, with intentional light blocking. The resulting transfer plots are shown in Figure 11. As expected, the direction of bias related shifts are toward positive voltages as indicated by the black arrow in the top left pane. This positive shift is expected from previous studies which argued that under positive bias stress a-IGZO forms oxygen-related electron-trapping (acceptor-like) states.[57] All four IXZO TFT classes exhibit a fall in I_{off} over the

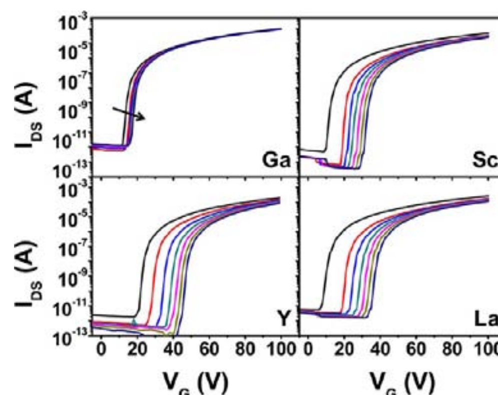

Figure 11. Effect of the gate bias stress on the transfer characteristics for IXZO TFTs with an In:X:Zn atomic ratio = 72.5:7.5:20 and T_{anneal} = 300 °C. Gate-to-drain bias +20 V was maintained for 200 s between transfer measurements for 1200 s.

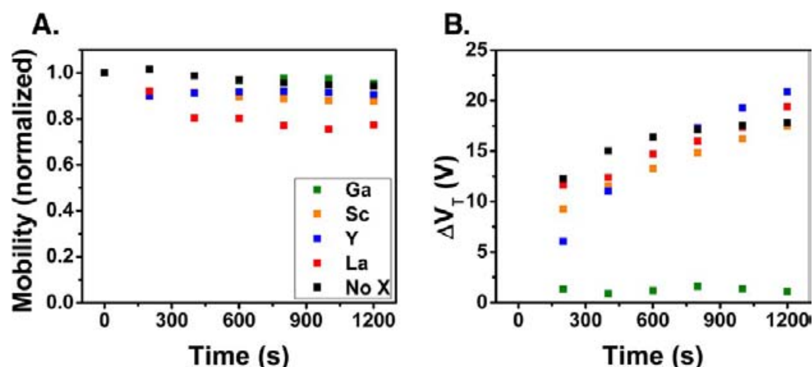

Figure 12. Effect of positive gate bias stress on field-effect mobility normalized to the initial value (A) and threshold voltage shift (B) for IXZO TFTs with In:X:Zn = 72.5:7.5:20 or 70:0:30; T_{anneal} = 300 °C. The 20 V gate-to-drain bias is maintained for 200 s between transfer measurements for 1200 s total.

bias duration, although the fall is significantly more limited in the case of IGZO devices. The threshold voltage for each system lies within the typical range observed for IXZO TFTs investigated in this study. In general, the best-performing TFTs having films prepared with each oxygen getter (X) at both film processing temperatures exhibit V_T's in the range of 10−25 V, with a positive shift observed with increasing X concentration. Figure 12 presents a comparison of the normalized mobility (A) and change in threshold voltage (ΔV_T) versus bias time (B). In terms of mobility, the IGZO TFTs show a slight but significant difference versus the other X metal cations, with a mobility retention of >95% of the initial value. In contrast, the ILZO devices perform the most poorly, with a mobility drop to 76% of the prebias stress value. In Figure 12B, a drastic difference is observed for IGZO when comparing ΔV_T to the other three systems. For ISZO, an initial shift of ∼9 V is followed by ∼1.5−2 V for each successive measurement. IYZO exhibits a smaller initial shift of ∼6 V, but maintains larger steps of 2−5 V after additional bias stress. The ILZO TFTs suffer the largest initial shift of ∼12 V, followed by an approximately 1 V additional shift per 200 s stress. In marked contrast, the IGZO-based TFTs exhibit excellent positive bias stress ΔV_T stability with an initial shift of only 1.3 V, and never exceeding 1.6 V. Interestingly, while IZO devices exhibit negligible mobility degradation they suffer severe V_T shifts, similar to those observed for the group 3 metal doped devices (Figures 12, S18).

It is likely that some contribution to the bias-related mobility and threshold voltage instability is caused by surface adsorbed O_2 and H_2O on the back channel, especially considering that these IXZO films are only ∼12 nm thick. However, the relatively good stability of the IGZO devices suggests that this contribution does not limit the ability to make an instructive comparison between the IXZO systems. The passivation of IXZO TFTs with a variety of solution-processable organic and inorganic encapsulants is currently under investigation.

■ DISCUSSION

Using crystalline IGZO as a model system, Hosono et al. argued that oxygen vacancies in amorphous oxide semiconductors play different roles, depending on where they are located in the local structure.[22a,23c] Specifically, if an oxygen vacancy is located at an edge- or face-sharing site, where large degrees of metal cation coordination are possible, then shallow donor states are formed. However, if the oxygen vacancy site is coordinated by only a small number of metal cations, in either a corner-sharing location or adjacent to an open space, then deep and/or shallow trap states are formed. Shallow trap states are known to correlate with a positive ΔV_T. Therefore, while oxygen vacancies are doubtlessly essential in amorphous oxide semiconductors to generate free carriers, careful control of their concentration and structural origin are also of utmost importance.

For the above reasons, we systematically explored composition effects in the IXZO series where X = Ga^{3+}, Sc^{3+}, Y^{3+}, and La^{3+} to better understand the role of the oxygen getter. A direct comparison of these different oxide films can be made based on AFM (Figure 6), GIAXRD (Figure 4), and HAADF-STEM (Figure 5) analysis and demonstrate that all film compositions remain highly amorphous with smooth surfaces. Therefore, comparison of $\eta_{M\text{-}O\text{-}M}$ differences is essential for determining the role of the oxygen getter in these systems and how it relates to the electrical performance. For this reason, XPS analysis (Figure 8) is very important. While fitting the O1s peak is insufficient to determine the absolute oxygen vacancy concentration in an oxide film (or their location), quantification of the M-O-M concentration in relation to the other oxygen binding states provides an informative measure of the oxygen binding affinities of the various getter cations. An effective oxygen getter should increase the ratio of the lower energy M-O-M peak to the total O1s peak area ($\eta_{M\text{-}O\text{-}M}$). As shown in Figure 8B, the only metal cation that provides an increase in M-O-M concentration as compared to other oxygen binding states is Ga^{3+}. While Sc^{3+}, Y^{3+}, and La^{3+} may also bind oxygen strongly, it is reasonable to conclude that, among other factors, their large sizes cause excessive lattice disruption (see more below).

To explain the role of Ga^{3+} or other oxygen getters in IZO properties enhancement, some studies have postulated that metal ion electronegativity is the key determinant of oxygen getter efficacy. Note that some studies have argued that lower[62] electronegativity is desired, while others have argued that higher[35b] values better control oxygen vacancies. One reason that electronegativity is a poor metric to rationalize charge mobility in these systems is that it does not account for local environment. Based on the results of the present study, as discussed above, we argue that the metal oxide lattice enthalpy (ΔH_L)[63] is a more accurate predictor of oxygen getter efficacy in IXZO materials. For a given M_aO_b, ΔH_L is the enthalpy of formation of the solid oxide from the corresponding gaseous ions and can be calculated from measured lattice energy values (U_{pot}).[64] Calorimetric experiments show for a number of metal

oxide systems that the energies of crystallization are roughly two orders of magnitude lower (~20 kJ/mol) than the lattice enthalpies discussed here (~6000−9000 kJ/mol).[65] This small difference between amorphous and crystalline states as compared to the much larger lattice enthalpies justifies their relevance in the present discussion. Furthermore, previous work has demonstrated the applicability of U_{pot} to amorphous systems.[66] Figure 13 compares literature ΔH_L values for each

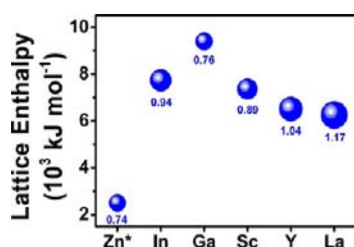

Figure 13. Lattice enthalpy values for various M_2O_3 compounds.[63a] Symbols are scaled to the eight-coordinate ionic radius of each metal ion in its preferred oxidation state with labeled values in Å. *Note: Zn lattice enthalpy is scaled to 1.5 oxygen bonds per Zn to match other metals.

oxygen getter in the form M_2O_3 (the value of ZnO has been normalized to 1.5 O per metal).[67] The symbol sizes in Figure 13 are scaled to the eight-coordinate ionic radius[52] of each X^{n+} ion with values also listed next to the points in Å. Note that Ga_2O_3 has a lattice enthalpy almost 1700 kJ mol^{-1} greater than any of the other oxides shown. In addition, Ga^{3+} has an ionic radius significantly smaller than that of In^{3+} and similar to that of Zn^{2+}. Conversely, with the exception of Sc, the other trivalent oxygen getters all have ionic radii larger than those of In^{3+} and Zn^{2+}. For example, the ionic radius of La^{3+} compared to In^{3+} is over 50% larger (0.41 Å). Although the group 3 metals all possess ΔH_L values larger than Zn^{2+}, all are less than that of In^{3+} and significantly less than that of Ga^{3+}. In addition their larger sizes may cause local structure disruption, hindering charge transport. The trends shown in Figure 13 also correlate excellently with the XPS O1s spectral analysis of Figure 8. Thus, the large ionic sizes and smaller ΔH_L values are consistent with the depressed TFT performance of the X = Sc^{3+}, Y^{3+}, and La^{3+} IXZO films compared to the analogous X = Ga^{3+} materials. Similarly, in the bias stress analysis in Figure 12, La is seen to perform poorest in terms of mobility retention while Sc and Y and are essentially the same and all three group 3 metals perform equally poorly in terms of V_T shift. This is not surprising considering that the difference in lattice enthalpy between Ga and the group 3 metals is very large whereas the difference among the group 3 metals is much less. From this analysis, other cations of similar size and having ΔH_L values comparable or greater than that of Ga^{3+}, such as Al^{3+}, Cr^{3+}, and Mn^{3+}, are predicted to be effective oxygen getters in IZO.[68]

Although a significant enhancement in IXZO TFT performance metrics is observed in the present study versus analogous sol−gel-derived films, X = Ga^{3+} clearly provides the best results, with μ as high as 5.5 cm^2 V^{-1} s^{-1}, good V_T considering the thick/low-κ gate dielectric[69] used (17 V), and excellent I_{on}/I_{off} values at T_{anneal} = 300 °C. Even at T_{anneal} = 250 °C, a temperature compatible with many inexpensive plastic substrates, combustion-derived a-IGZO films still exhibit an impressive μ = 1.3 cm^2 V^{-1} s^{-1}. In comparison, the other X getter metal ions at T_{anneal} = 300 °C yield μ = 1.8−2.6 cm^2 V^{-1} s^{-1} under optimized processing and compositional conditions. Note that all of the present X ions have larger ΔH_L values than Zn^{2+} (Figure 13), which is beneficial for lattice formation and electron transport, but ultimately the TFT performance appears to be a balance between ionic radii and ΔH_L. Note also that the trends in Figure 13 correlate closely with the XPS O1s peak analysis of Figure 8, and the superior $\eta_{M\text{-}O\text{-}M}$ of Ga^{3+} is completely consistent with the aforementioned trends in ΔH_L and ionic radius. Similarly, the bias stress data in Figure 12 also correlate with these trends, which show the superior bias stress stability of the X = Ga^{3+}-based films.

■ CONCLUSIONS

This report presents the first systematic experimental study of the carrier suppression role of X ions in amorphous IXZO thin films.[62] A detailed microstructural and electrical comparison of various oxygen getters in solution/combustion-processed amorphous oxide IXZO semiconductors is reported. A large phase space of each metal composition at T_{anneal} = 250 and 300 °C is scrutinized, enabled by the ease of composition variation using low-temperature combustion processing. AFM, X-ray diffraction, and TFT characterization reveal ultrasmooth, amorphous, high mobility films at all compositions and processing temperatures. STEM with HAADF imaging confirms the amorphicity of these films and indicates significant nanoporosity for all four oxygen getters. X-ray photoelectron spectroscopy reveals a significant difference in O1s binding between Ga^{3+} and the other trivalent X cations. Specifically, only Ga^{3+} increases the M−O−M content at high doping concentrations, consistent with the "oxygen getter" function. In contrast, Sc^{3+}, Y^{3+}, and La^{3+} all have larger ionic radii versus In^{3+} and Zn^{2+} and so appear to act as effective amorphicizing agents but not as strong oxygen binders. Thin-film transistors fabricated on SiO_2 gate dielectrics support these conclusions, with IGZO-based TFTs exhibiting much higher electron mobilities than those for the other X ion dopants. Furthermore, positive bias stress measurements reveal IGZO TFTs to be impressively stable in both $\Delta\mu_{sat}$ and ΔV_T with maximum deviations of only 5% and 1.6 V, respectively. In contrast, ISZO, IYZO, and ILZO TFTs show large $\Delta\mu_{sat}$ values in the range of 10−22% and ΔV_T from 17 to 20 V after a 1200 s bias. We believe that these insights will aid in understanding the role of strong oxygen binding metal cations in solution-processed amorphous metal oxide electronics, hence advancing technologies based upon them.

■ EXPERIMENTAL SECTION

Combustion Precursor Preparation and Characterization. All combustion precursor materials were purchased from Sigma-Aldrich and used without further purification. For the combustion precursor preparation, each metal nitrate salt (176.1 mg of $In(NO_3)_3{\cdot}xH_2O$; 148.6 mg of $Zn(NO_3)_2{\cdot}6H_2O$; 199.8 mg of $Ga(NO_3)_3{\cdot}xH_2O$; 160.6 mg of $Sc(NO_3)_2{\cdot}5H_2O$; 173.5 mg of $Y(NO_3)_3{\cdot}4H_2O$; 216.6 mg of $La(NO_3)_2{\cdot}6H_2O$) was dissolved in 10 mL of 2-methoxyethanol before the addition of 55 μL of 14.5 M NH_3 (aq) and 100 μL of acetylacetone and allowed to stir for 12 h. Approximately 1 h prior to spin-coating, the combustion precursor solutions were combined by micropipet to desired molar ratios and stirred. Precursor solutions were prepared for thermal analysis by removal of solvent by applying a vacuum while heating the solutions at 70 °C in an oil bath. TGA and DTA were performed on 10−15 mg samples by using a Mettler 851e instrument under air with a flow rate of 20 mL/min and a heating ramp rate of 10 °C/min from 25 to 600 °C.

Thin Film Fabrication and Structural Characterization. IXZO solutions of desired molar ratio were spin-coated on n++ Si wafers (WRS Materials; solvent cleaned and then cleaned with an oxygen plasma for 5 min) at 3500 rpm for 30 s in a dry air glovebox (CleaTech) and subsequently annealed for 20 min at 250 or 300 °C for each layer. This process was repeated three times to obtain the desired film thickness. Surface roughness was measured with a Veeco Dimension ICON PT AFM System in tapping mode with a silicon cantilever (AppNano). Grazing incidence X-ray diffraction was carried out with a Rigaku ATX-G Thin-Film Diffraction Workstation using Cu Kα radiation coupled to a multilayer mirror. X-ray photoelectron spectroscopy was performed on a Thermo Scientific ESCALAB 250 Xi spectrometer at a base pressure of 4.5×10^{-10} mbar (UHV). XPS spectra were obtained immediately after film fabrication in order to minimize surface contamination. Oxygen 1s spectra were fitted using three Gaussian−Lorentzian Product peak functions after subtracting a linear baseline. The peak amplitude, width, and shape coefficient were used as fitting parameters while the peak positions were fixed within a certain range, depending on the particular binding energy. Areas were then calculated for each of the deconvoluted peaks. TEM samples were prepared following the procedures described above, but instead of spin-coating they were inkjet printed onto quantifoil SiN_x membrane substrates, on which the free-standing IXZO films were processed by a previously described method.[17a] TEM characterization was carried out on a JEOL 2100 S/TEM at the accelerating voltage of 200 keV.

Transistor Fabrication and Electrical Characterization. Bottom-gate/top-contact field-effect transistors were fabricated on n ++ Si/SiO_2 (300 nm thermal oxide, WRS Materials) by spin-coating and annealing the combustion precursor solution as described above. To reduce parasitic gate currents, the semiconductor film was removed ~2 mm around all edges of the substrate using an acid etch. Substrates were soaked for 30 s in 10% oxalic acid solution (w/v in DI water, VWR) after masking with wafer dicing tape (Semiconductor Equipment Corporation). Any tape residue was then removed by sonication in ethanol, followed by a 30 min anneal at the desired temperature in 40% relative humidity. Aluminum source/drain electrodes were deposited by thermal evaporation (Denton Vacuum Explorer) at a rate of ~1 Å/s through a shadow mask to afford channel dimensions $W = 5000$ μm and $L = 100$ μm. Current−voltage (I−V) transfer and output measurements were conducted on a Signatone probe station with a Keithley 6430 subfemtoamp remote source meter and a Keithley 2400 source meter using a locally written LabVIEW program. All electrical characterizations were conducted in ambient without intentional light blocking. TFT performance metrics, including saturation mobility (μ_{sat}), threshold voltage (V_T), and current on/off ratio (I_{on}/I_{off}), were evaluated using the standard TFT model described in eq 1.

ASSOCIATED CONTENT

Supporting Information

Raw XRD, XPS data with fitting parameters, AFM of IZO films, and TFT performance metrics for IZO. This information is available free of charge via the Internet at http://pubs.acs.org.

AUTHOR INFORMATION

Corresponding Author

v-dravid@northwestern.edu (V.P.D.); a-facchetti@northwestern.edu (A.F.); t-marks@northwestern.edu (T.J.M.)

Notes

The authors declare no competing financial interest.

ACKNOWLEDGMENTS

We thank ONR (MURI N00014-11-1-0690), the Northwestern University Materials Research Science and Engineering Center (NSF DMR-1121262), and Polyera Corp. for support of this research. Microscopy studies were performed in the NIFTI and KECK II facilities of NUANCE Center at Northwestern University. NUANCE is supported by NSF-NSEC, NSF-MRSEC, Keck Foundation, the State of Illinois, and Northwestern University. We also thank Prof. T. O. Mason for helpful discussions.

REFERENCES

(1) (a) Kim, Y.-H.; Heo, J.-S.; Kim, T.-H.; Park, S.; Yoon, M.-H.; Kim, J.; Oh, M. S.; Yi, G.-R.; Noh, Y.-Y.; Park, S. K. *Nature* **2012**, *489*, 128−132. (b) Jeong, S.; Moon, J. *J. Mater. Chem.* **2012**, *22*, 1243−1250. (c) Fortunato, E.; Barquinha, P.; Martins, R. *Adv. Mater.* **2012**, *24*, 2945−2986. (d) Kola, S.; Sinha, J.; Katz, H. E. *J. Polym. Sci. Pol. Phys.* **2012**, *50*, 1090−1120. (e) *Transparent Electronics*; Marks, T. J., Facchetti, A., Eds.; VCH-Wiley: West Sussex U.K., 2010. (f) Medvedeva, J. E. *Appl. Phys. A: Mater. Sci. Process* **2007**, *89*, 43−47. (g) Nomura, K.; Ohta, H.; Takagi, A.; Kamiya, T.; Hirano, M.; Hosono, H. *Nature* **2004**, *432*, 488−492.

(2) (a) Kim, K. M.; Kim, C. W.; Heo, J.-S.; Na, H.; Lee, J. E.; Park, C. B.; Bae, J.-U.; Kim, C.-D.; Jun, M.; Hwang, Y. K.; Meyers, S. T.; Grenville, A.; Keszler, D. A. *Appl. Phys. Lett.* **2011**, *99*, 242109−3. (b) Kumar, A.; Zhou, C. *ACS Nano* **2010**, *4*, 11−14. (c) Kamiya, T.; Nomura, K.; Hosono, H. *Sci. Technol. Adv. Mater.* **2010**, *11*, 044305. (d) Grover, M. S.; Hersh, P. A.; Chiang, H. Q.; Kettenring, E. S.; Wager, J. F.; Keszler, D. A. *J. Phys. D: Appl. Phys.* **2007**, *40*, 1335. (e) Hayashi, R.; Ofuji, M.; Kaji, N.; Takahashi, K.; Abe, K.; Yabuta, H.; Sano, M.; Kumomi, H.; Nomura, K.; Kamiya, T.; Hirano, M.; Hosono, H. *J. Soc. Inf. Display* **2007**, *15*, 915−921. (f) Kamiya, T.; Hiramatsu, H.; Nomura, K.; Hosono, H. *J. Electroceram.* **2006**, *17*, 267−275. (g) Gulino, A.; Castelli, F.; Dapporto, P.; Rossi, P.; Fragalà, I. *Chem. Mater.* **2002**, *14*, 704−709.

(3) http://www.sharpsma.com/press/2013/Sharp-IGZO-based-LCD-and-OLED-Displays-Show-Display-Week-2013.

(4) *Technology and Applications of Amorphous Silicon*; Street, R. A., Ed.; Springer-Verlag: Berlin, Germany, 2000.

(5) (a) Segura, J. L.; Herrera, H.; Bauerle, P. *J. Mater. Chem.* **2012**, *22*, 8717−8733. (b) Usta, H.; Facchetti, A.; Marks, T. J. *Acc. Chem. Res.* **2011**, *44*, 501−510. (c) Sokolov, A. N.; Tee, B. C. K.; Bettinger, C. J.; Tok, J. B. H.; Bao, Z. *Acc. Chem. Res.* **2011**, *45*, 361−371. (d) Hu, L.; Hecht, D. S.; Grüner, G. *Chem. Rev. (Washington, DC, U. S.)* **2010**, *110*, 5790−5844. (e) Schwierz, F. *Nat. Nanotechnol.* **2010**, *5*, 487−496. (f) Jariwala, D.; Sangwan, V. K.; Lauhon, L. J.; Marks, T. J.; Hersam, M. C. *Chem. Soc. Rev.* **2013**, *42*, 2824−60. (g) Marks, T J. *MRS Bull.* **2010**, *35*, 1018−1027.

(6) (a) Gao, Z. Q.; Mi, B. X.; Xu, G. Z.; Wan, Y. Q.; Gong, M. L.; Cheah, K. W.; Chen, C. H. *Chem. Commun. (Cambridge, U. K.)* **2008**, 117−119. (b) Tse Nga, N.; Chabinyc, M. L.; Street, R. A.; Salleo, A. *Proc. IEEE Int. Rel. Phys. Symp.* **2007**, 243−247.

(7) (a) Sun, D.-m.; Timmermans, M. Y.; Tian, Y.; Nasibulin, A. G.; Kauppinen, E. I.; Kishimoto, S.; Mizutani, T.; Ohno, Y. *Nat. Nanotechnol.* **2011**, *6*, 156−161. (b) Sangwan, V. K.; Ortiz, R. P.; Alaboson, J. M. P.; Emery, J. D.; Bedzyk, M. J.; Lauhon, L. J.; Marks, T. J.; Hersam, M. C. *ACS Nano* **2012**, *6*, 7480−7488. (c) Shastry, T. A.; Seo, J.-W. T.; Lopez, J. J.; Arnold, H. N.; Kelter, J. Z.; Sangwan, V. K.; Lauhon, L. J.; Marks, T. J.; Hersam, M. C. *Small* **2012**, *9*, 45−51.

(8) Arnold, M. S.; Green, A. A.; Hulvat, J. F.; Stupp, S. I.; Hersam, M. C. *Nat. Nanotechnol.* **2006**, *1*, 60−65.

(9) Park, H.; Afzali, A.; Han, S. J.; Tulevski, G. S.; Franklin, A. D.; Tersoff, J.; Hannon, J. B.; Haensch, W. *Nat. Nanotechnol.* **2012**, *7*, 787−91.

(10) (a) Wan, X.; Long, G.; Huang, L.; Chen, Y. *Adv. Mater.* **2011**, *23*, 5342−5358. (b) Lin, Y.-M.; Dimitrakopoulos, C.; Jenkins, K. A.; Farmer, D. B.; Chiu, H.-Y.; Grill, A.; Avouris, P. *Science* **2010**, *327*, 662.

(11) (a) Liu, J.; Buchholz, D. B.; Chang, R. P. H.; Facchetti, A.; Marks, T. J. *Adv. Mater.* **2010**, *22*, 2333−2337. (b) Liu, J.; Buchholz, D. B.; Hennek, J. W.; Chang, R. P. H.; Facchetti, A.; Marks, T. J. *J. Am. Chem. Soc.* **2010**, *132*, 11934−11942. (c) Liu, J.; Hennek, J. W.; Buchholz, D. B.; Ha, Y.-G.; Xie, S.; Dravid, V. P.; Chang, R. P. H.; Facchetti, A.; Marks, T. J. *Adv. Mater.* **2011**, *23*, 992−997.

(12) Yabuta, H.; Sano, M.; Abe, K.; Aiba, T.; Den, T.; Kumomi, H.; Nomura, K.; Kamiya, T.; Hosono, H. *Appl. Phys. Lett.* **2006**, *89*, 112123.
(13) Hosono, H. *Active-Matrix Flatpanel Displays and Devices (AM-FPD), 19th International Workshop on* **2012**, 1−4.
(14) (a) Kim, H. S.; Kim, M.-G.; Ha, Y.-G.; Kanatzidis, M. G.; Marks, T. J.; Facchetti, A. *J. Am. Chem. Soc.* **2009**, *131*, 10826−10827. (b) Rim, Y. S.; Lim, H. S.; Kim, H. J. *ACS Appl. Mater. Interfaces* **2013**, *5*, 3565−3571.
(15) Cheng, H.-C.; Chen, C.-F.; Lee, C.-C. *Thin Solid Films* **2006**, *498*, 142−145.
(16) Choi, Y.; Kim, G. H.; Jeong, W. H.; Kim, H. J.; Chin, B. D.; Yu, J.-W. *Thin Solid Films* **2010**, *518*, 6249−6252.
(17) (a) Hennek, J. W.; Xia, Y.; Everaerts, K.; Hersam, M. C.; Facchetti, A.; Marks, T. J. *ACS Appl. Mater. Interfaces* **2012**, *4*, 1614−1619. (b) Kim, G. H.; Kim, H. S.; Shin, H. S.; Ahn, B. D.; Kim, K. H.; Kim, H. J. *Thin Solid Films* **2009**, *517*, 4007−4010. (c) Lee, D. H.; Chang, Y. J.; Herman, G. S.; Chang, C. H. *Adv. Mater.* **2007**, *19*, 843−847.
(18) Banger, K. K.; Yamashita, Y.; Mori, K.; Peterson, R. L.; Leedham, T.; Rickard, J.; Sirringhaus, H. *Nat. Mater.* **2011**, *10*, 45−50.
(19) Kim, M.-G.; Kanatzidis, M. G.; Facchetti, A.; Marks, T. J. *Nat. Mater.* **2011**, *10*, 382−388.
(20) Hennek, J. W.; Kim, M.-G.; Kanatzidis, M. G.; Facchetti, A.; Marks, T. J. *J. Am. Chem. Soc.* **2012**, *134*, 9593−9596.
(21) Kim, M.-G.; Hennek, J. W.; Kim, H. S.; Kanatzidis, M. G.; Facchetti, A.; Marks, T. J. *J. Am. Chem. Soc.* **2012**, *134*, 11583−11593.
(22) (a) Kamiya, T.; Nomura, K.; Hosono, H. *Phys. Status Solidi A* **2009**, *206*, 860−867. (b) Orita, M.; Tanji, H.; Mizuno, M.; Adachi, H.; Tanaka, I. *Phys. Rev. B* **2000**, *61*, 1811−1816.
(23) (a) Noh, H.-K.; Chang, K. J.; Ryu, B.; Lee, W.-J. *Phys. Rev. B* **2011**, *84*, 115205. (b) Omura, H.; Kumomi, H.; Nomura, K.; Kamiya, T.; Hirano, M.; Hosono, H. *J. Appl. Phys.* **2009**, *105*, 093712. (c) Kamiya, T.; Nomura, K.; Hirano, M.; Hosono, H. *Phys. Status Solidi C* **2008**, *5*, 3098−3100. (d) Exarhos, G. J.; Windisch, C. F., Jr; Ferris, K. F.; Owings, R. R. *Appl. Phys. A: Mater. Sci. Process* **2007**, *89*, 9−18.
(24) (a) Hopper, E. M.; Peng, H.; Hawks, S. A.; Freeman, A. J.; Mason, T. O. *J. Appl. Phys.* **2012**, *112*, 093712. (b) Lany, S.; Zunger, A. *Phys. Rev. Lett.* **2007**, *98*, 045501. (c) Tomita, T.; Yamashita, K.; Hayafuji, Y.; Adachi, H. *Appl. Phys. Lett.* **2005**, *87*, 051911-3.
(25) (a) Conley, J. F. *IEEE Trans. Device Mater. Rel.* **2010**, *10*, 460−475. (b) Lee, J.-M.; Cho, I.-T.; Lee, J.-H.; Cheong, W.-S.; Hwang, C.-S.; Kwon, H.-I. *Appl. Phys. Lett.* **2009**, *94*, 222112.
(26) Paine, D. C.; Yaglioglu, B.; Beiley, Z.; Lee, S. *Thin Solid Films* **2008**, *516*, 5894−5898.
(27) Hwang, Y. H.; Jeon, J. H.; Seo, S.-J.; Bae, B.-S. *Electrochem. Solid-State Lett.* **2009**, *12*, H336−H339.
(28) Jeong, S.; Jeong, Y.; Moon, J. *J. Phys. Chem. C* **2008**, *112*, 11082−11085.
(29) (a) Yao, Q.; Li, S.; Zhang, Q. *Appl. Surf. Sci.* **2011**, *258*, 1460−1463. (b) Chong, H. Y.; Han, K. W.; No, Y. S.; Kim, T. W. *Appl. Phys. Lett.* **2011**, *99*, 161908.
(30) Oh, B.-Y.; Park, J.-C.; Lee, Y.-J.; Cha, S.-J.; Kim, J.-H.; Kim, K.-Y.; Kim, T.-W.; Heo, G.-S. *J. Solid State Chem.* **2011**, *184*, 2462−2465.
(31) Park, J. C.; Kim, S. W.; Kim, C. J.; Lee, H.-N. *IEEE Electron Device Lett.* **2012**, *33*, 809−811.
(32) Yoon, D. H.; Kim, S. J.; Jeong, W. H.; Kim, D. L.; Rim, Y. S.; Kim, H. J. *J. Cryst. Growth* **2011**, *326*, 171−174.
(33) (a) Chong, E.; Chun, Y. S.; Lee, S. Y. *Appl. Phys. Lett.* **2010**, *97*, 102102−3. (b) Chong, E.; Kim, S. H.; Lee, S. Y. *Appl. Phys. Lett.* **2010**, *97*, 252112−3.
(34) (a) Kim, D.-H.; Son, D.-H.; Sung, S.-J.; Kim, J.-H.; Kang, J.-K. *Mol. Cryst. Liq. Cryst.* **2012**, *564*, 130−137. (b) Park, J.-S.; Kim, K.; Park, Y.-G.; Mo, Y.-G.; Kim, H. D.; Jeong, J. K. *Adv. Mater.* **2009**, *21*, 329−333.
(35) (a) Chong, E.; Chun, Y. S.; Kim, S. H.; Lee, S. Y. *Thin Solid Films* **2011**, *519*, 6881−6883. (b) Chang-Jung, K.; Sangwook, K.; Je-Hun, L.; Jin-Seong, P.; Sunil, K.; Jaechul, P.; Eunha, L.; Jaechul, L.; Youngsoo, P.; Joo Han, K.; Sung Tae, S.; Chung, U.-I. *Appl. Phys. Lett.* **2009**, *95*, 252103. (c) Jeong, W. H.; Kim, G. H.; Kim, D. L.; Shin, H. S.; Kim, H. J.; Ryu, M.-K.; Park, K.-B.; Seon, J.-B.; Lee, S.-Y. *Thin Solid Films* **2011**, *519*, 5740−5743.
(36) (a) Choi, Y.; Kim, G. H.; Jeong, W. H.; Bae, J. H.; Kim, H. J.; Hong, J.-M.; Yu, J.-W. *Appl. Phys. Lett.* **2010**, *97*, 162102. (b) Qadri, S. B.; Kim, H. *J. Appl. Phys.* **2002**, *92*, 227−229.
(37) Shin, H. S.; Kim, G. H.; Jeong, W. H.; Du Ahn, B.; Kim, H. J. *Jpn. J. Appl. Phys.* **2010**, *49*, 03CB01.
(38) Kim, D. N.; Kim, D. L.; Kim, G. H.; Kim, S. J.; Rim, Y. S.; Jeong, W. H.; Kim, H. J. *Appl. Phys. Lett.* **2010**, *97*, 192105.
(39) Koo, C. Y.; Song, K.; Jung, Y.; Yang, W.; Kim, S.-H.; Jeong, S.; Moon, J. *ACS Appl. Mater. Interfaces* **2012**, *4*, 1456−1461.
(40) (a) Kim, Y.-H.; Han, M.-K.; Han, J.-I.; Park, S. K. *IEEE Trans. Electron Devices* **2010**, *57*, 1009−1014. (b) Kim, D.; Koo, C. Y.; Song, K.; Jeong, Y.; Moon, J. *Appl. Phys. Lett.* **2009**, *95*, 103501−3.
(41) Edwards, P. P.; Porch, A.; Jones, M. O.; Morgan, D. V.; Perks, R. M. *Dalton Trans.* **2004**, 2995−3002.
(42) (a) Ono, S.; Yamane, M.; Okushima, H.; Koguchi, M.; Shinada, H.; Kakibayashi, H.; Yano, F.; Tsunomura, T.; Nishida, A.; Mogami, T. *Appl. Phys. Express* **2011**, *4*, 066601−066603. (b) Jeon, H.; Na, S.; Moon, M. R.; Jung, D.; Kim, H.; Lee, H. J. *J. Electrochem. Soc.* **2011**, *158*, H949−H954. (c) Pal, B.; Sharon, M. *Mater. Chem. Phys.* **2002**, *76*, 82−87. (d) Brinker, C. J.; Scherer, G. W. *Sol-gel science: the physics and chemistry of sol-gel processing*; Academic Press: Boston, 1990.
(43) Yang, P.; Zhao, D.; Margolese, D. I.; Chmelka, B. F.; Stucky, G. D. *Nature* **1998**, *396*, 152−155.
(44) Chung, W.-F.; Chang, T.-C.; Li, H.-W.; Chen, S.-C.; Chen, Y.-C.; Tseng, T.-Y.; Tai, Y.-H. *Appl. Phys. Lett.* **2011**, *98*, 152109−3.
(45) Donley, C.; Dunphy, D.; Paine, D.; Carter, C.; Nebesny, K.; Lee, P.; Alloway, D.; Armstrong, N. R. *Langmuir* **2001**, *18*, 450−457.
(46) Nomura, K.; Kamiya, T.; Hirano, M.; Hosono, H. *Appl. Phys. Lett.* **2009**, *95*, 013502−3.
(47) (a) Dupin, J.-C.; Gonbeau, D.; Vinatier, P.; Levasseur, A. *Phys. Chem. Chem. Phys.* **2000**, *2*, 1319−1324. (b) Takeda, S.; Fukawa, M.; Hayashi, Y.; Matsumoto, K. *Thin Solid Films* **1999**, *339*, 220−224. (c) McCafferty, E.; Wightman, J. P. *Surf. Interface Anal.* **1998**, *26*, 549−564. (d) Stoch, J.; Gablankowska-Kukucz, J. *Surf. Interface Anal.* **1991**, *17*, 165−167.
(48) (a) Kwo, J.; Hong, M.; Kortan, A. R.; Queeney, K. L.; Chabal, Y. J.; Opila, J. R. L.; Muller, D. A.; Chu, S. N. G.; Sapjeta, B. J.; Lay, T. S.; Mannaerts, J. P.; Boone, T.; Krautter, H. W.; Krajewski, J. J.; Sergnt, A. M.; Rosamilia, J. M. *J. Appl. Phys.* **2001**, *89*, 3920−3927. (b) Lavalley, J. C. *Catal. Today* **1996**, *27*, 377−401. (c) Gervasini, A.; Auroux, A. *J. Catal.* **1991**, *131*, 190−198. (d) Auroux, A.; Gervasini, A. *J. Phys. Chem.* **1990**, *94*, 6371−6379.
(49) Kamiya, T.; Nomura, K.; Hosono, H. *J. Display Technol.* **2009**, *5*, 273−288.
(50) Okamura, K.; Nikolova, D.; Mechau, N.; Hahn, H. *Appl. Phys. Lett.* **2009**, *94*, 183503−3.
(51) Wang, Y.; Sun, X. W.; Goh, G. K. L.; Demir, H. V.; Hong, Y. Y. *IEEE Trans. Electron Devices* **2011**, *58*, 480−485.
(52) Shannon, R. D. *Acta Crystallogr. A* **1976**, *32*, 751−767.
(53) Nomura, K.; Kamiya, T.; Ohta, H.; Hirano, M.; Hosono, H. *Appl. Phys. Lett.* **2008**, *93*, 192107−3.
(54) (a) Barquinha, P.; Vila, A. M.; Goncalves, G.; Pereira, L.; Martins, R.; Morante, J. R.; Fortunato, E. *IEEE Trans. Electron Devices* **2008**, *55*, 954−960. (b) Seo, S.-J.; Hwang, Y. H.; Bae, B.-S. *Electrochem. Solid-State Lett.* **2010**, *13*, H357−H359.
(55) Street, R. A. *Adv. Mater.* **2009**, *21*, 2007−2022.
(56) Seo, O.; Chung, J.; Jo, J. *Eur Phys J-Appl Phys* **2011**, *54*, 10302−10305.
(57) Chen, W.-T.; Lo, S.-Y.; Kao, S.-C.; Zan, H.-W.; Tsai, C.-C.; Lin, J.-H.; Fang, C.-H.; Lee, C.-C. *IEEE Electron Device Lett.* **2011**, *32*, 1552−1554.
(58) Seo, H.-S.; Bae, J.-U.; Kim, D.-H.; Park, Y.; Kim, C.-D.; Kang, I. B.; Chung, I.-J.; Choi, J.-H.; Myoung, J.-M. *Electrochem. Solid-State Lett.* **2009**, *12*, H348−H351.

(59) Olziersky, A.; Barquinha, P.; Vila, A.; Pereira, L.; Goncalves, G.; Fortunato, E.; Martins, R.; Morante, J. R. *J. Appl. Phys.* **2010**, *108*, 064505−7.
(60) Choi, S.-H.; Jang, J.-H.; Kim, J.-J.; Han, M.-K. *IEEE Electron Device Lett.* **2012**, *33*, 381−383.
(61) Sung, S. Y.; Choi, J. H.; Han, U. B.; Lee, K. C.; Lee, J. H.; Kim, J. J.; Lim, W.; Pearton, S. J.; Norton, D. P.; Heo, Y. W. *Appl. Phys. Lett.* **2010**, *96*, 102107.
(62) Kim, D. L.; Jeong, W. H.; Kim, G. H.; Kim, H. J. *J. Inform. Disp.* **2012**, *13*, 113−118.
(63) (a) Wagman, D. D.; Evans, W. H.; Parker, V. B.; Schumm, R. H.; Halow, I.; Bailey, S. M.; Churney, K. L.; Nuttall, R. L. *J. Phys. Chem. Ref. Data* **1989**, *18*, 1807−1812. (b) Jenkins, H. D. B.; Pratt, K. F. In *Advances in Inorganic Chemistry and Radiochemistry*; Emeléus, H. J., Sharpe, A. G., Eds.; Academic Press: 1979; Vol. *22*, pp 1−111.
(64) (a) Cotton, F. A. *Advanced Inorganic Chemistry*, 6th ed.; Wiley: New York, 1999. (b) Jenkins, H. D. B.; Roobottom, H. K.; Passmore, J.; Glasser, L. *Inorg. Chem.* **1999**, *38*, 3609−3620.
(65) (a) Radha, A. V.; Forbes, T. Z.; Killian, C. E.; Gilbert, P. U.; Navrotsky, A. *Proc. Natl. Acad. Sci. U.S.A.* **2010**, *107*, 16438−43. (b) Zhou, W.; Ushakov, S. V.; Wang, T.; Ekerdt, J. G.; Demkov, A. A.; Navrotsky, A. *J. Appl. Phys.* **2010**, *107*, 123514−7. (c) Lamoreaux, R. H. H., D. L. *J. Phys. Chem. Ref. Data* **1984**, *13*, 151−173. (d) Ushakov, S. V.; Navrotsky, A.; Yang, Y.; Stemmer, S.; Kukli, K.; Ritala, M.; Leskela, M. A.; Fejes, P.; Demkov, A.; Wang, C.; Nguyen, B. Y.; Triyoso, D.; Tobin, P. *Physica Status Solidi B* **2004**, *241*, 2268−2278. (e) Ciuparu, D.; Ensuque, A.; Shafeev, G.; Bozon-Verduraz, F. *J. Mater. Sci. Lett.* **2000**, *19*, 931−933. (f) Navrotsky, A. *J. Chem. Thermodyn.* **2007**, *39*, 1−9.
(66) Glasser, L.; Jenkins, H. D. B. *J. Am. Chem. Soc.* **2000**, *122*, 632−638.
(67) (a) Bush, T. S.; Gale, J. D.; Catlow, C. R. A.; Battle, P. D. *J. Mater. Chem.* **1994**, *4*, 831−837. (b) Jenkins, H. D. B.; Tudela, D.; Glasser, L. *Inorg. Chem.* **2002**, *41*, 2364−2367.
(68) *CRC Handbook of Chemistry and Physics*, 73rd ed.; CRC Press: Boca Raton, FL, 1992.
(69) (a) Ortiz, R. P.; Facchetti, A.; Marks, T. J. *Chem. Rev.* **2010**, *110*, 205−239. (b) DiBenedetto, S. A.; Facchetti, A.; Ratner, M. A.; Marks, T. J. *Chem. Rev.* **2009**, *21*, 1407−1433.